Finite Elements in Analysis and Design 47 (2011) 635–642

Contents lists available at ScienceDirect

Finite Elements in Analysis and Design

journal homepage: www.elsevier.com/locate/finel

Bi-dimensional finite element analysis for modal separation of a circular cylindrical WW-USM

Tai-Ho Yu, Shin-Yueh Yang, Chen-Liang Lee, Ching-Chung Yin *

Department of Mechanical Engineering, National Chiao Tung University, 1001 Ta Hsueh Road, Hsinchu 30010, Taiwan, Republic of China

ARTICLE INFO

Article history:
Received 7 August 2010
Accepted 23 January 2011
Available online 19 February 2011

Keywords:
Wedge wave ultrasonic motor (WW-USM)
Bi-dimensional finite element analysis (Bi-d FEA) method
Modal separation
Modal sensors

ABSTRACT

This paper describes a modal separation model that improves the performance of wedge wave ultrasonic motors (WW-USMs) using the bi-dimensional finite element analysis (Bi-d FEA) method. Most USMs operate near the resonant frequency of a specific vibration mode, which must be well separated from the resonant frequencies of other modes. In the current prototype, unexpected disturbance induced at the instant of switching on/off or changing direction of the motor appeared in simulations and actual measurements. These fluctuations are due to vibration modes other than the driving mode occurring around the operating frequency. Bi-d FEA numerical simulation results indicate that selecting an appropriate height for the upper base under the piezoelectric tube achieves excellent modal separation. Measurements of the traveling wave taken by modal sensors show that the proposed motor performs better than traditional motors, offering a faster transient response in revolution speed and a more stable design. Suppressing the unexpected modes in excitation of the WW-USM increased the maximum output torque by 50% and the efficiency of mechanical/electrical transformation by 50%.

1. Introduction

Lagasse [1] and Lagasse et al. [2] were the first to discover acoustic wedge waves in 1972. Wedge waves carry most of their elastic energy within the area of about one wavelength from the wedge tip. The phase velocity of the acoustic wedge waveguide is slower than its material Rayleigh wave, and dispersion free under no truncation situation. In 1994 and 2007, Krylov [3] and Krylov and Pritchard [4,5] proposed a geometrical acoustics theory to test the guided wave propagation speed on a wedge tip under the water. Analysis results show that the phase velocity under the water is slower than that in the air due to the coupling effect of the water. Hladky-Hennion [6] developed a bi-dimensional mathematical model in 1996 to study the propagation of acoustic waves in waveguides. The problem is reduced to a 2-dimensional problem, where only the cross-section of the guide is mesh using finite elements. They presented a theoretical formulation for the cases of the linear and circular waveguide neglected the piezoelectric effects. This paper adds the piezoelectric effect into the bi-dimensional mathematical model to develop a circular cylindrical WW-USM and improve the performance of ultrasonic motors.

Ultrasonic motors (USMs) are called piezoelectric motors because they are driven by piezoelectric actuators. Ultrasonic mechanical vibrations induce traveling waves around the motor stator and frictional force between the contact surfaces that push the rotor or slider. Compared with electro-magnetic motors, USMs have superior characteristics in several aspects, including a simple structure, high torque at low revolution speed, freedom from electro-magnetic interference and high controllability. Researchers have developed various types of USM over the past four decades. Existing designs generally fall into several geometric types of piezoceramic ultrasonic actuators: ring-type [7,8], cylinder-type [9–11], disk-type [12–16], hollow cylinder-type [17–21], etc. Most studies on this topic focus on the steady state response and performance, and relatively few researchers have investigated the transient response of the USM. The transient response reflects the participation of resonant modes near the driving mode.

Fig. 1 shows the schematic view of a WW-USM. The fourth fundamental flexural mode $F(1, 4)$, traveling circumferentially around the wedge, drives the motor in this. However, several unexpected modes near the operating frequency accompany the flexural mode. Uncertain transient disturbances appear at the instant of switching on/off or changing motor direction. Adjusting the upper segment height of the stepped base achieves excellent modal separation near the driving frequency.

This study improves the performance of the WW-USM using the bi-dimensional finite element analysis (Bi-d FEA) method. Structural vibration analysis reveals the entire frequency response function of the stator. The response corresponding to

* Corresponding author.
E-mail address: ccyin@faculty.nctu.edu.tw (C.-C. Yin).

0168-874X/$ - see front matter © 2011 Elsevier B.V. All rights reserved.
doi:10.1016/j.finel.2011.01.006

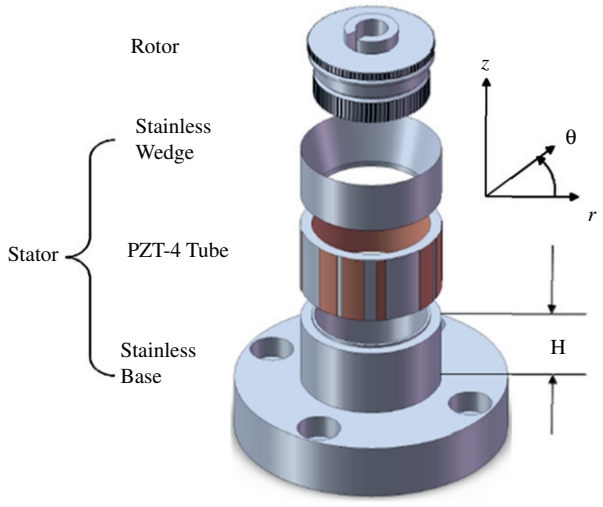

Fig. 1. Exploded view of the WW-USM.

each vibration mode must be compared through modal analysis of the commercial code ANSYS. Experimental results show that good modal separation achieves a faster response and stable revolution speed.

2. Bi-dimensional finite element analysis (Bi-d FEA)

2.1. Piezoelectric constitutive equation

The piezoelectric ceramic material used in this paper is PZT-4, which is a 6-mm crystal system and transversely isotropic material. Under an electric field and mechanical force load, the piezoelectric constitutive equation is

$$\mathbf{T}=\mathbf{c}^E\mathbf{S}-\mathbf{e}^T\mathbf{E}$$
$$\mathbf{D}=\mathbf{e}\mathbf{S}+\boldsymbol{\varepsilon}^S\mathbf{E} \tag{2.1}$$

where **T** and **S** are the stress matrix and strain matrix, respectively, $\mathbf{c}^E$ is the elastic stiffness matrix, **e** is the piezoelectric constant matrix, **D** is the electric displacement, **E** is the electric field intensity and $\boldsymbol{\varepsilon}^S$ is the dielectric constant matrix under constant strain. This study assumes that the cylindrical coordinate (r, z, θ) and the piezoelectric tube is polarized in a radial direction.

The elastic stiffness matrix is

$$\mathbf{c}=\begin{bmatrix} C_{33} & C_{13} & C_{13} & 0 & 0 & 0 \\ C_{13} & C_{11} & C_{12} & 0 & 0 & 0 \\ C_{13} & C_{12} & C_{11} & 0 & 0 & 0 \\ 0 & 0 & 0 & C_{66} & 0 & 0 \\ 0 & 0 & 0 & 0 & C_{44} & 0 \\ 0 & 0 & 0 & 0 & 0 & C_{44} \end{bmatrix} \tag{2.2}$$

The piezoelectric constant matrix is

$$\mathbf{e}=\begin{bmatrix} e_{33} & e_{31} & e_{31} & 0 & 0 & 0 \\ 0 & 0 & 0 & 0 & 0 & e_{15} \\ 0 & 0 & 0 & 0 & e_{15} & 0 \end{bmatrix} \tag{2.3}$$

The dielectric constant matrix is

$$\boldsymbol{\varepsilon}^S=\begin{bmatrix} \varepsilon_{33}^S & 0 & 0 \\ 0 & \varepsilon_{11}^S & 0 \\ 0 & 0 & \varepsilon_{11}^S \end{bmatrix} \tag{2.4}$$

The following equations define the stress matrix **T**, strain matrix **S**, displacement vector **u**, electric displacement **D**, electric field density **E** and electric potential **Φ**

$$\mathbf{T}=\begin{bmatrix}\sigma_{rr} & \sigma_{zz} & \sigma_{\theta\theta} & \sigma_{z\theta} & \sigma_{r\theta} & \sigma_{rz}\end{bmatrix}^T \tag{2.5}$$

$$\mathbf{S}=\begin{bmatrix}\varepsilon_{rr} & \varepsilon_{zz} & \varepsilon_{\theta\theta} & 2\varepsilon_{z\theta} & 2\varepsilon_{r\theta} & 2\varepsilon_{rz}\end{bmatrix}^T \tag{2.6}$$

$$\mathbf{u}=\begin{bmatrix}u_r & u_z & u_\theta\end{bmatrix}^T \tag{2.7}$$

$$\mathbf{D}=\begin{bmatrix}D_r & D_z & D_\theta\end{bmatrix}^T \tag{2.8}$$

$$\mathbf{E}=\begin{bmatrix}E_r & E_z & E_\theta\end{bmatrix}^T \tag{2.9}$$

$$\boldsymbol{\Phi}=\{\Phi\} \tag{2.10}$$

2.2. Hamilton's principle

The surface traction and surface charge of a guided wave tube may be zero at any part. In classical mechanics, the Lagrangian function L of all the pertinent variables (the independent coordinates and velocities) is

$$L=T-H \tag{2.11}$$

where T is the kinetic energy and H is the enthalpy. The internal kinetic energy is

$$T=\frac{1}{2}\int_\theta\int_z\int_r \dot{\mathbf{u}}^H\boldsymbol{\rho}\dot{\mathbf{u}}\,r\,dr\,dz\,d\theta \tag{2.12}$$

The enthalpy is the difference between the strain energy and the electric potential

$$H=\frac{1}{2}\int_\theta\int_z\int_r(\mathbf{S}^H\mathbf{c}\mathbf{S}-\mathbf{S}^H\mathbf{e}^H\mathbf{E}-\mathbf{E}^H\mathbf{e}\mathbf{S}-\mathbf{E}^H\boldsymbol{\varepsilon}^S\mathbf{E})r\,dr\,dz\,d\theta \tag{2.13}$$

where $\boldsymbol{\rho}$ is the density of the elastic wave guided and is a (3×3) diagonal matrix, the over dot represents the partial differential of the time and the upper H is a Hermitian matrix. If the material stiffness matrix **c** and density matrix $\boldsymbol{\rho}$ both are real symmetric matrices, the strain energy and the kinetic energy are positive definite. The Lagrangian function of the wave guided is then

$$L=\frac{1}{2}\int_\theta\int_z\int_r(\dot{\mathbf{u}}^H\boldsymbol{\rho}\dot{\mathbf{u}}-\mathbf{S}^H\mathbf{c}\mathbf{S}+\mathbf{S}^H\mathbf{e}^H\mathbf{E}+\mathbf{E}^H\mathbf{e}\mathbf{S}+\mathbf{E}^H\boldsymbol{\varepsilon}^S\mathbf{E})r\,dr\,dz\,d\theta \tag{2.14}$$

Hamilton's principle indicates that under the conditions of no external force and surface electric charge, integrating the Lagrangian function with time leads to

$$\int_{t_1}^{t_2}\delta(T-H)\,dt=\delta\int_{t_1}^{t_2}L\,dt=0 \tag{2.15}$$

In the interval ($t1$, $t2$), the first derivative of all field variables is zero.

2.3. Dispersion equation

This study adopts the Bi-d FEA method to determine the resonant vibration modes and phase velocities of circumferentially flexural waves. The structure of the motor stator includes several 2-dimensional discrete four-node isoparametric (Q4) elements, as Fig. 2 shows. The elastic displacements **u** and electric

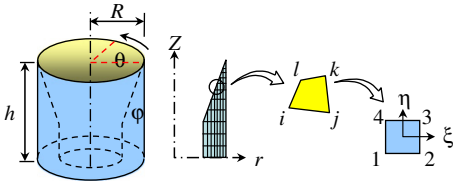

Fig. 2. The Bi-d FEA of the WW-USM stator.

potential $\mathbf{\Phi}$ are

$$\mathbf{u}=\begin{Bmatrix} u_r \\ u_z \\ u_\theta \end{Bmatrix}=\begin{Bmatrix} u_r(r,z,t)) \\ u_z(r,z,t) \\ ju_\theta(r,z,t) \end{Bmatrix}e^{jn\theta} \tag{2.16}$$

$$\mathbf{\Phi}=\varphi=\varphi(r,z,t)e^{jn\theta} \tag{2.17}$$

where the circumferential mode number $n=kR$, k is a wave number, $j=\sqrt{-1}$ and $e^{jn\theta}$ is the wave propagation factor. The number n is a non-integer for traveling waves, but may be an integer for a standing wave. The matrices $\mathbf{N}_u$, $\mathbf{N}_\phi$ consist of the interpolation functions corresponding to nodal displacements and electric potential.

The elastic displacements $\mathbf{u}$ and electric potential $\mathbf{\Phi}$ at a point inside each element can be interpolated by the nodal displacement $\mathbf{d}$ and nodal electric potential $\boldsymbol{\varphi}$ in the form

$$\mathbf{u}=\mathbf{N}_u\mathbf{d} \tag{2.18}$$

$$\mathbf{\Phi}=\mathbf{N}_\phi\boldsymbol{\varphi} \tag{2.19}$$

where

$$\mathbf{u}=\begin{bmatrix} u_r & u_z & u_\theta \end{bmatrix}^T \tag{2.20}$$

$$\mathbf{\Phi}=\{\Phi\} \tag{2.21}$$

$$\mathbf{N}_u=\begin{bmatrix} \mathbf{N}_1 & \mathbf{N}_2 & \mathbf{N}_3 & \mathbf{N}_4 \end{bmatrix} \tag{2.22}$$

$$\mathrm{N}_i=\begin{bmatrix} N_i & 0 & 0 \\ 0 & N_i & 0 \\ 0 & 0 & jN_i \end{bmatrix}e^{jn\theta} \tag{2.23}$$

$$\mathbf{N}_\phi=N_ie^{jn\theta} \tag{2.24}$$

$$N_i=\frac{1}{4}(1+\xi\xi_i)(1+\eta\eta_i) \tag{2.25}$$

$$\mathbf{d}=\begin{bmatrix} \mathbf{d}_1 & \mathbf{d}_2 & \mathbf{d}_3 & \mathbf{d}_4 \end{bmatrix}^T \tag{2.26}$$

$$\mathbf{d}_i=\begin{bmatrix} u_r^i & u_z^i & u_\theta^i \end{bmatrix} \tag{2.27}$$

$$\boldsymbol{\varphi}=\begin{bmatrix} \phi^1 & \phi^2 & \phi^3 & \phi^4 \end{bmatrix}^T \tag{2.28}$$

The matrix forms of the element stress $\mathbf{S}$ and the element electric field intensity $\mathbf{E}$ are

$$\mathbf{S}=\mathbf{B}_u\mathbf{d} \tag{2.29}$$

$$\mathbf{E}=-\mathbf{B}_\varphi\boldsymbol{\varphi} \tag{2.30}$$

where

$$\mathbf{B}_u=\begin{bmatrix} \mathbf{B}_{u1} & \mathbf{B}_{u2} & \mathbf{B}_{u3} & \mathbf{B}_{u4} \end{bmatrix} \tag{2.31}$$

$$\mathbf{B}_{ui}=\begin{bmatrix} \partial N_i/\partial r & 0 & 0 \\ 0 & \partial N_i/\partial z & 0 \\ N_i/r & 0 & -n(N_i/r) \\ 0 & jn(N_i/r) & j(\partial N_i/\partial z) \\ jn(N_i/r) & 0 & j(\partial N_i/\partial r-N_i/r) \\ \partial N_i/\partial z & \partial N_i/\partial r & 0 \end{bmatrix}e^{jn\theta} \tag{2.32}$$

$$\mathbf{B}_\varphi=\begin{bmatrix} \mathbf{B}_{\varphi1} & \mathbf{B}_{\varphi2} & \mathbf{B}_{\varphi3} & \mathbf{B}_{\varphi4} \end{bmatrix} \tag{2.33}$$

$$\mathbf{B}_{\varphi i}=\begin{bmatrix} \partial N_i/\partial r \\ \partial N_i/\partial z \\ jn(N_i/r) \end{bmatrix}e^{jn\theta} \tag{2.34}$$

Note that u_θ has a 90° phase lag to the other two elastic displacement components. The total kinetic energy T, the enthalpy H and the Lagrangian function L are

$$T=\frac{1}{2}\sum\dot{\mathbf{d}}^H\mathbf{m}\dot{\mathbf{d}} \tag{2.35}$$

$$H=\frac{1}{2}\sum(\mathbf{d}^H\mathbf{k}_{uu}\mathbf{d}+\mathbf{d}^H\mathbf{k}_{u\varphi}\boldsymbol{\varphi}+\boldsymbol{\varphi}^H\mathbf{k}_{\varphi u}\mathbf{d}-\boldsymbol{\varphi}^H\mathbf{k}_{\varphi\varphi}\boldsymbol{\varphi}) \tag{2.36}$$

$$L=T-H=\frac{1}{2}\sum(\dot{\mathbf{d}}^H\mathbf{m}\dot{\mathbf{d}}-\mathbf{d}^H\mathbf{k}_{uu}\mathbf{d}-\mathbf{d}^H\mathbf{k}_{u\varphi}\boldsymbol{\varphi}-\boldsymbol{\varphi}^H\mathbf{k}_{\varphi u}\mathbf{d}+\boldsymbol{\varphi}^H\mathbf{k}_{\varphi\varphi}\boldsymbol{\varphi}) \tag{2.37}$$

Using Hamilton's principle and substituting Eqs. (2.35)–(2.37) into Eq. (2.15) leads to

$$\delta\sum\int_{t1}^{t2}\left\{\frac{1}{2}(\dot{\mathbf{d}}^H\mathbf{m}\dot{\mathbf{d}}-\mathbf{d}^H\mathbf{k}_{uu}\mathbf{d}-\mathbf{d}^H\mathbf{k}_{u\varphi}\boldsymbol{\varphi}-\boldsymbol{\varphi}^H\mathbf{k}_{\varphi u}\mathbf{d}+\boldsymbol{\varphi}^H\mathbf{k}_{\varphi\varphi}\boldsymbol{\varphi})\right\}dt=0 \tag{2.38}$$

Consider from t_1 to t_2, set $\delta\mathbf{d}^H=\delta\mathbf{d}=0$ and integration by part, from Eq. (2.38) the variational principle takes the form

$$\begin{aligned}\frac{1}{2}\sum\Big\{&\delta\mathbf{d}^H\int_{t_1}^{t_2}(\mathbf{m}\ddot{\mathbf{d}}+\mathbf{k}_{uu}\mathbf{d}+\mathbf{k}_{u\varphi}\boldsymbol{\varphi})\,dt+\delta\boldsymbol{\varphi}^H\int_{t_1}^{t_2}(\mathbf{k}_{\varphi u}\mathbf{d}+\mathbf{k}_{\varphi\varphi}\boldsymbol{\varphi})\,dt\\&+\int_{t_1}^{t_2}(\ddot{\mathbf{d}}^H\mathbf{m}+\mathbf{d}^H\mathbf{k}_{uu}+\boldsymbol{\varphi}^H\mathbf{k}_{\varphi u})\,dt\,\delta\mathbf{d}\\&+\int_{t_1}^{t_2}(\mathbf{d}^H\mathbf{k}_{u\varphi}+\boldsymbol{\varphi}^H\mathbf{k}_{\varphi\varphi})\,dt\,\delta\boldsymbol{\varphi}\Big\}=0\end{aligned} \tag{2.39}$$

Hence, the motion equations of the guided wave are

$$\sum\left\{\mathbf{m}\ddot{\mathbf{d}}+\mathbf{k}_{uu}\mathbf{d}+\mathbf{k}_{u\varphi}\boldsymbol{\varphi}\right\}=0 \tag{2.40}$$

$$\sum\left\{\mathbf{k}_{\varphi u}\mathbf{d}+\mathbf{k}_{\varphi\varphi}\boldsymbol{\varphi}\right\}=0 \tag{2.41}$$

$$\sum\left\{\ddot{\mathbf{d}}^T\mathbf{m}+\mathbf{d}^T\mathbf{k}_{uu}+\boldsymbol{\varphi}^T\mathbf{k}_{\varphi u}\right\}=0 \tag{2.42}$$

$$\sum\left\{\mathbf{d}^T\mathbf{k}_{u\varphi}+\boldsymbol{\varphi}^T\mathbf{k}_{\varphi\varphi}\right\}=0 \tag{2.43}$$

where the element mass matrix $\mathbf{m}$, the element stiffness matrices $\mathbf{k}_{uu}$, $\mathbf{k}_{u\varphi}$, $\mathbf{k}_{\varphi u}$ and $\mathbf{k}_{\varphi\varphi}$ are symmetry matrices. Thus, Eq. (2.40) equals Eq. (2.42), and Eq. (2.41) equals Eq. (2.43). Then, we obtain the element's equation of motion in matrix form is

$$\sum\left(\begin{bmatrix} \mathbf{m} & 0 \\ 0 & 0 \end{bmatrix}\begin{Bmatrix} \ddot{\mathbf{d}} \\ \ddot{\boldsymbol{\varphi}} \end{Bmatrix}+\begin{bmatrix} \mathbf{k}_{uu} & \mathbf{k}_{u\varphi} \\ \mathbf{k}_{\varphi u} & \mathbf{k}_{\varphi\varphi} \end{bmatrix}\begin{Bmatrix} \mathbf{d} \\ \boldsymbol{\varphi} \end{Bmatrix}\right)=\mathbf{0} \tag{2.44}$$

Finally, a global system of motion equations for wedge waves traveling along the circular cylindrical stator is as follows:

$$\begin{bmatrix} \mathbf{M} & 0 \\ 0 & 0 \end{bmatrix}\begin{Bmatrix} \ddot{\mathbf{D}} \\ \ddot{\mathbf{\Phi}} \end{Bmatrix}+\begin{bmatrix} \mathbf{K}_{uu} & \mathbf{K}_{u\varphi} \\ \mathbf{K}_{\varphi u} & \mathbf{K}_{\varphi\varphi} \end{bmatrix}\begin{Bmatrix} \mathbf{D} \\ \mathbf{\Phi} \end{Bmatrix}=\begin{Bmatrix} 0 \\ 0 \end{Bmatrix} \tag{2.45}$$

where $\mathbf{M}$, $\mathbf{K}_{uu}$, $\mathbf{K}_{u\varphi}$, $\mathbf{K}_{\varphi\varphi}$ are the global mass matrix, global elastic, elasto-piezoelectric and piezoelectric stiffness matrices. Assuming that all the field quantities are time-harmonic and $e^{-i\omega t}$ is the time-harmonic factor. Let $\mathbf{D}=\overline{\mathbf{D}}e^{-i\omega t}$, $\ddot{\mathbf{D}}=-\omega^2\overline{\mathbf{D}}e^{-i\omega t}$, $\mathbf{\Phi}=\overline{\mathbf{\Phi}}e^{-i\omega t}$ and $\ddot{\mathbf{\Phi}}=-\omega^2\overline{\mathbf{\Phi}}e^{-i\omega t}$ substitute into Eq. (2.45) to obtain

$$\left(\begin{bmatrix} \mathbf{K}_{uu} & \mathbf{K}_{u\varphi} \\ \mathbf{K}_{\varphi u} & \mathbf{K}_{\varphi\varphi} \end{bmatrix}-\omega^2\begin{bmatrix} \mathbf{M} & 0 \\ 0 & 0 \end{bmatrix}\right)\begin{Bmatrix} \overline{\mathbf{D}} \\ \overline{\mathbf{\Phi}} \end{Bmatrix}=0 \tag{2.46}$$

The existence of the nontrivial solution to Eq. (2.46) produces the following the dispersion equation or frequency equation:

$$\det\left(\begin{bmatrix} \mathbf{K}_{uu} & \mathbf{K}_{u\varphi} \\ \mathbf{K}_{\varphi u} & \mathbf{K}_{\varphi\varphi} \end{bmatrix}-\omega^2\begin{bmatrix} \mathbf{M} & \mathbf{0} \\ \mathbf{0} & \mathbf{0} \end{bmatrix}\right)=0 \tag{2.47}$$

It is possible to calculate the resonant modes of flexural waves using the angular frequency $\omega=2\pi f$ and the circumferential wave

number $k=n/R$ in Eq. (2.47). The term R represents the radius of a circular wedge.

3. Simulation results

Fig. 3 shows the structure and sizes of the original motor stator. The motor stator consists of a cylindrical metal wedge, a piezoelectric tube and a two-segment stepped metal base. The piezoelectric tube has an inner diameter, outer diameter and height of 21.9, 25.9 and 12.5 mm, respectively. The piezoelectric tube in this study is made of PZT-4 supplied by Eleceram Inc. in Taiwan, and has the following charge coefficients: $d_{33}=289$ pC/N and $d_{31}=-123$ pC/N. The height of the circular wedge is 9.44 mm and the wedge angle is 15°. The height of the lower-segment base is 10 mm. Both the circular wedge and the two-segment base are made of stainless steel (mass density $\rho=7.82$ g/cm^3, Young modulus $E=201.25$ GPa and Poisson ratio $\sigma=0.29$). All components are adhered together. The flexural mode of interest in this WW-USM drives the ultrasonic motor. The term $F(m, n)$ represents the flexural mode, where m and n are the numbers of the radial modes and circumference modes on the stator, respectively. The elastic waves traveling along the circumference of the motor stator consist of the interference of the two flexural vibrations of the same modes. In the prototype manufactured for the performance test, fourth fundamental flexural mode $F(1,4)$ traveling circumferentially around the wedge drove the motor. The piezoelectric tube was poled radially through its thickness from the inside to the outside. The electrodes were placed over one half of each wavelength circumferentially around the tube, as Fig. 4 shows. Modal sensors were employed to measure the driving frequencies and dynamic response of the WW-USM during operation.

The Bi-d FEA method allows precise and efficient numerical calculation for waveguide propagation of the motor stator for both the traveling wave (n is a non-integer) and the standing wave (n is an integer). The program used in this study was written in the FORTRAN computer language. The motor stator of the upper-segment base height $H=0$ was meshed by 1900 elements, 2081 nodes and 26 nodes constrained on the bottom, as Fig. 5(a) shows. The motor stator of the upper-segment base height $H=12.5$ mm was meshed by 2050 elements, 2241 nodes and 26 nodes constrained on the bottom, as Fig. 5(b) shows.

Comparative numerical calculations for vibration of the motor stator were carried out using commercial code ANSYS 10.0 (ANSYS Inc., Canonsburg, PA, USA). An element type of SOLID 5 was selected. The motor stator of $H=0$ contains 60,440 elements and 73,200 nodes, with 420 fixed nodes on the bottom of the stepped base, as Fig. 6(a) shows. The motor stator of $H=12.5$ mm contains 80,440 elements and 89,200 nodes, with 420 fixed nodes on the bottom of the stepped base, as Fig. 6(b) shows.

Fig. 7 shows the dispersion curve of the two type motor stator by Bi-d FEA and ANSYS. The Bi-d FEA result indicates that the frequency difference between the flexural mode $F(1,4)$ ($f_r=36.099$) and $F(2,2)$

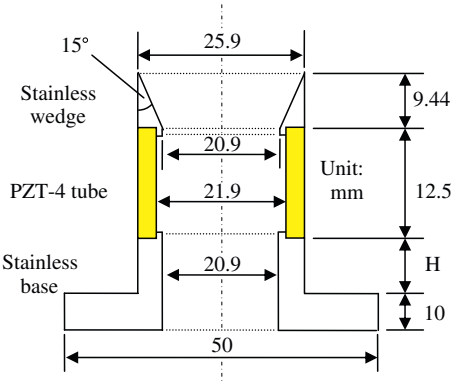

Fig. 3. Sectional view of the WW-USM stator.

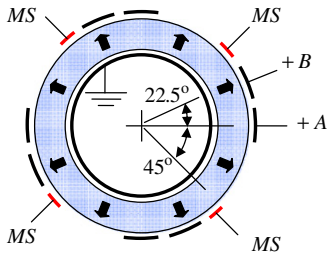

Fig. 4. Top view of the dual-phase electrodes (+A, +B) exerted by two 90° out-of-phase alternating voltages and integrated modal sensors (MS) placed on the outer surface of the PZT tube (the arrow indicates the poling direction).

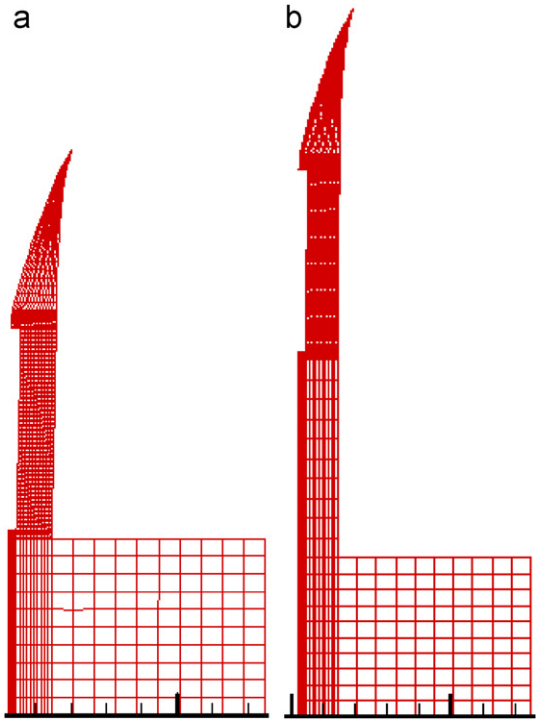

Fig. 5. Resonant modes of the WW-USM stator by the Bi-d FEA (a) flexural mode $F(1,4)$ for $H=0$ ($f_r=36.099$ kHz) (b) flexural mode $F(1,4)$ for $H=12.5$ mm ($f_r=36.008$ kHz).

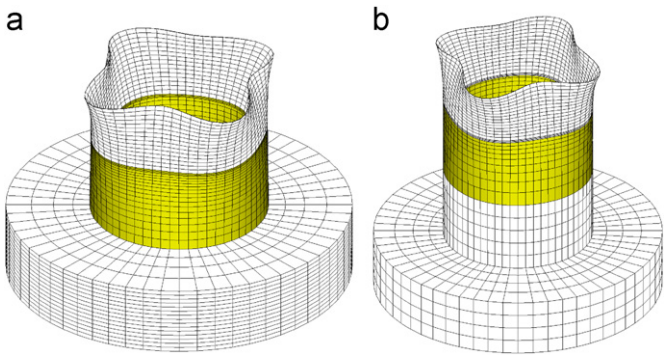

Fig. 6. Resonant modes of the WW-USM stator by the ANSYS (a) flexural mode $F(1,4)$ for $H=0$ ($f_r=36.095$ kHz) (b) flexural mode $F(1,4)$ for $H=12.5$ mm ($f_r=36.058$ kHz).

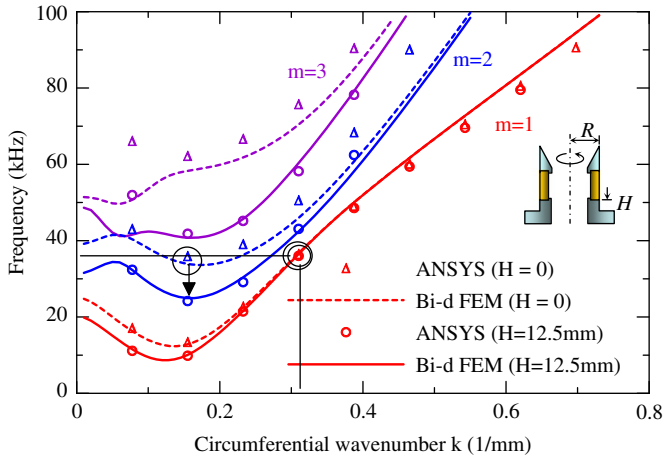

Fig. 7. Dispersion curve of circumferential wave number and frequency (where the double circle represents the $F(1,4)$ mode, i.e. $k=n/R=4/12.95=0.309$ and $f_r=36.008$ kHz. The single circle represents the $F(2,2)$ mode, $f_r=35.742$ kHz. The arrow represents the resonant frequency decreases about 11.6 kHz).

Table 1
Resonant frequencies of the WW-USM stator by Bi-d FEA simulation with an upper segment base height $H=12.5$ mm (the values enclosed in parentheses are those for $H=0$).

	Resonant frequency (kHz)		
n	$m=1$	$m=2$	$m=3$
1	11.138 (17.146)	32.308 (43.118)	51.940 (66.441)
2	9.849 (13.492)	24.142 (35.742)	41.813 (62.234)
3	21.448 (22.780)	29.140 (39.139)	45.174 (66.711)
4	36.008 (36.099)	43.084 (50.617)	58.193 (75.798)
5	48.559 (49.169)	62.442 (68.442)	78.227 (90.492)

($f_r=35.742$ kHz) is only 357 Hz if the upper base height $H=0$. Both modes were stimulated simultaneously very easily if $H=0$, inducing disturbance at the instant of switching on/off or changing the direction of the motor. On the other hand, if the upper base height $H=12.5$ mm, the frequency difference between the $F(1,4)$ mode ($f_r=36.008$ kHz) and the nearest $F(2,1)$ mode ($f_r=32.308$ kHz) was 3.7 kHz. The mode $F(2,2)$ resonant frequency became 24.142 kHz, which is far from the mode $F(1,4)$. This is the best modal separation available in the WW-USM structure design.

Table 1 shows the resonant frequencies of the WW-USM stator with base height $H=12.5$ mm and $H=0$ according to the Bi-d FEA method. The following experiments selected $H=0$ and $H=12.5$ mm to fabricate two prototypes of the WW-USM and measure its performance around the operation frequency. The rotor was made of Nary Brass (mass density $\rho=8.47$ g/cm^3, Young modulus $E=105.46$ GPa and Poisson ratio $\sigma=0.34$). The rotor border was embossed with teeth-like structures on the contact point to increase contact and friction force.

4. Experimental results

Two prototypes of the WW-USM were fabricated and Fig. 8 presents their photos. Dynamic displacements of the motor stator were measured by a laser Doppler vibrometer (LDV) system ONO SOKKI LV-1720A (ONO SOKKI Corp., Tokyo, Japan), as Fig. 9 shows. the thin solid line in this figure indicates the spectrum of WW-USM in $H=0$, while the thick dashed line represents the spectrum of WW-USM in $H=12.5$ mm. Experimental measurement results show that if $H=0$, the frequency difference between the flexural mode $F(1,4)$ ($f_r=36.108$ kHz) and $F(2,2)$ ($f_r=35.784$ kHz) is only

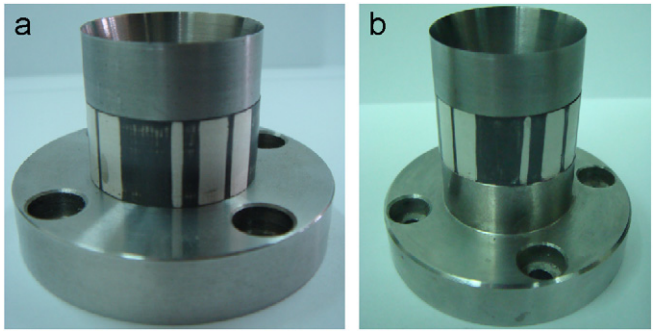

Fig. 8. The prototypes for WW-USM (a) $H=0$ (b) $H=12.5$ mm.

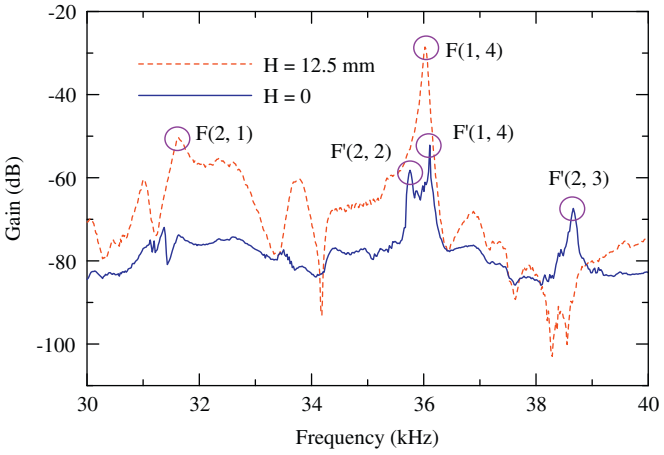

Fig. 9. Spectrum of the WW-USM by LDV (where $F'(m,n)$ represents the modes of $H=0$, $F(m,n)$ represents the modes of $H=12.5$ mm).

324 Hz. In this case, the two modes are very close, but also interfere with each other. The resonant frequency of the flexural mode $F(1,4)$ is $f_r=36.056$ kHz if the $H=12.5$ mm and no other neighbor modes exist in the frequency ranges of 3.7 kHz.

Fig. 10 shows the schematic setup for measuring the dynamic performance of the proposed WW-USM. A waveform generator Agilent 33250 A (Agilent Technologies, Santa Clara, CA, USA) generated a sine wave of driving frequency and amplitude 20 Vp-p. A phase shifter circuit separated the sine wave signal into dual-phase sine waves ($+10\sin(\omega t)$, $+10\cos(\omega t)$). Both signals were magnified up to 20 times the amplitude by two high voltage power operational amplifiers Apex PA90 (Cirrus Logic Inc., Austin, Texas, USA). Under a pre-load of 100 gW (include the rotor and spring) and a driving frequency of 36.108 kHz ($H=0$) or 36.056 kHz ($H=12.5$ mm), the dual-phase amplified AC signals were applied to the electrodes of the motor stator to induce the traveling wave on the wedge tip. The dual-phase driving signals and the reactive signals from modal sensors were simultaneously measured using a digital storage Oscilloscope LeCroy WS42Xs (LeCroy Corp., New York, USA), as Fig. 11 shows. The waveform was pure and stable if $H=12.5$ mm, but the waveform amplitude was small and exhibited a little noise and distortion if $H=0$.

During motor operation by friction force, the motor shaft coupling connection rotary axis drove the encoder (HRT-3A/1000 ppr, Hontko Inc., Taiwan) and determined the revolution speed. A load cell (LSM400, Futek Co., Taiwan) detected the rotary torque signal, while a Vishay 2210B signal conditioner (Vishay Micro-Measurement, Inc., Munich, Germany) amplified and filtered the signals. A NI-DAQ-PXI-6251 (National Instrument Co., Austin, Texas, USA) data acquisition interface recorded data on the revolution speed, rotary torque and reactive signal using

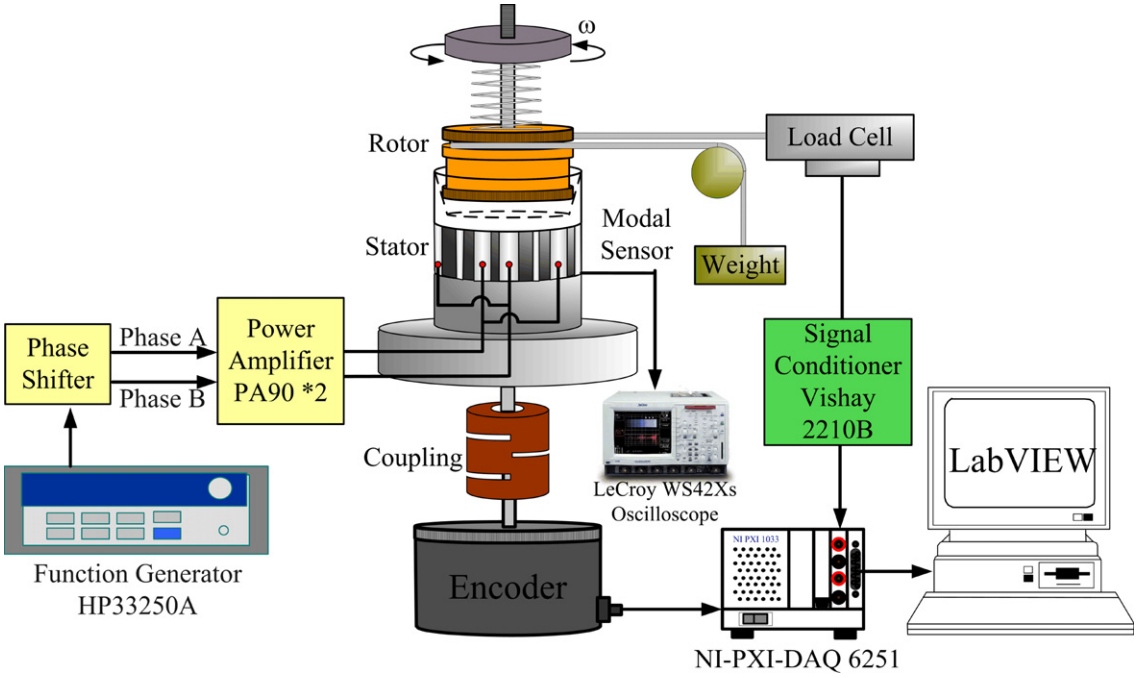

Fig. 10. Experimental setup of the WW-USM performance test.

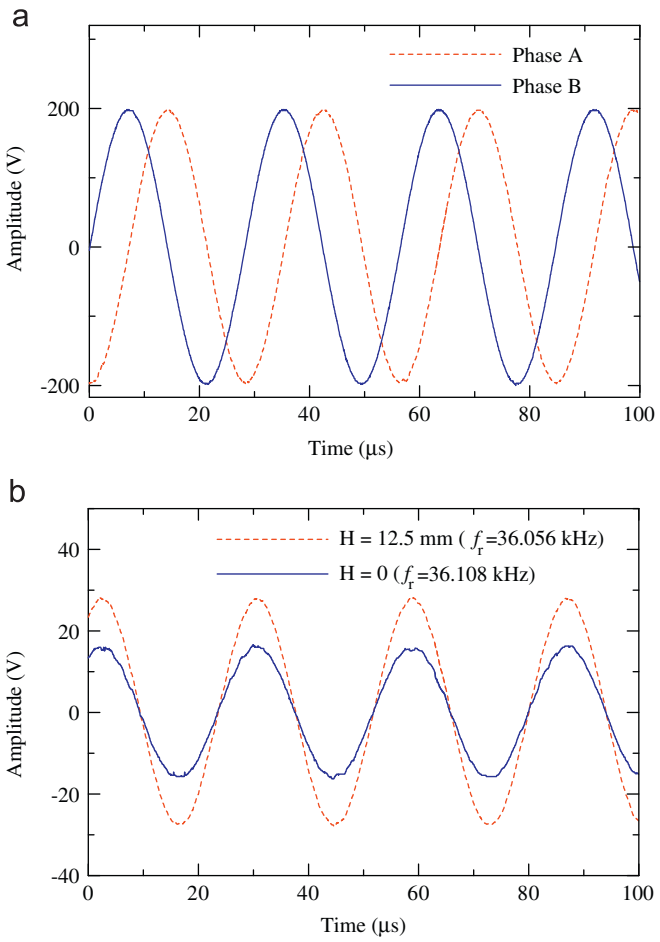

Fig. 11. The waveform of the dual-phase driving signals and the modal sensors (a) dual-phase driving signals (b) signals of the modal sensors (MS).

modal sensors. The NI-LabVIEW V8.5 package functioned as a supervisor program for the automatic measurement system, immediately measuring and presenting data in the monitor.

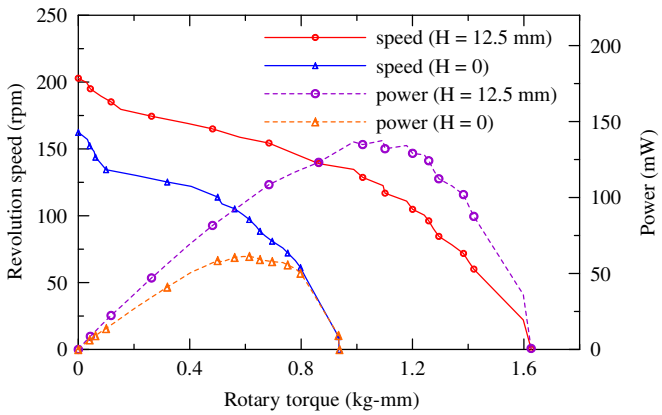

Fig. 12. WW-USM performance.

Fig. 12 shows the performance of the WW-USM. This figure indicates that the maximum revolution speed was 155 rpm and the maximum rotary torque was 0.93 kg mm when the upper segment base height of the stator was $H=0$. In contrast, the maximum revolution speed was 220 rpm and the maximum rotary torque was 1.62 kg mm when $H=12.5$ mm. Fig. 13 shows the transient response of the WW-USM. When $H=0$, the rise time of revolution speed was 89 ms and unstable chattering appeared in the steady state. However, the rise time decreased to 45 ms when $H=12.5$ mm. This indicates that the proposed structural design achieved quicker response and more stable steady state with excellent modal separation in the vicinity of the driving frequency.

5. Discussion

Because the analysis of the acoustic guide wave is one kinds of complex boundary value problem, the exact analytic solution of the wedge waveguide is not proposed yet. Only the simple experience formula by Lagasse et al. [2] and geometric acoustic

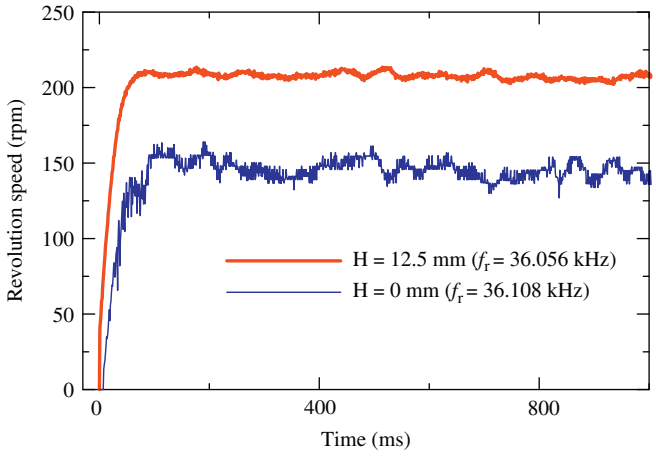

Fig. 13. Transient response of the WW-USM.

approximate solution by Krylov and Pritchard [4] were presented. The ideal linear wedge waveguide is infinite long base, but the actual circular wedge waveguide is impossible to have infinite long base. However, the generally commercial finite element package does not have the efficient and lack the precision in the analysis of linear or circular wedge waveguide. Therefore, in the design and application of the circular acoustic waveguide, the development of a numerical analysis method for calculated the phase velocity and dispersion curve of the flexural wave is absolutely necessary.

The Bi-d FEA method is a type of reduction process based on the finite element method. By reducing a 3-dimensional problem into a 2-dimensional problem, the Bi-d FEA method allows faster calculations while retaining 3-dimensional data. This is why this method is called bi-dimensional, and not 2-dimensional. This study uses the Bi-d FEA method to calculate the dispersion curve of the WW-USM stator including the data of phase speed c (mm/μs), resonant frequency f (kHz) and wave number k (1/mm). Numerical simulation results show that this method can calculate the 2D resonant mode shape, including the standing wave mode shape, if the circumferential mode number n is an integer and the traveling wave mode shape if n is a non-integer. However, the commercial codes ANSYS can only calculate the standing wave if n is integer. Clearly, the Bi-d FEA method has an advantage over the ANSYS package in terms of time and computer memory required.

The WW-USM is a motor driven by traveling wave and the friction force between the rotor and the stator. Therefore, confirming the resonant mode and its corresponding resonant frequency is an important task. The concept of modal separation changes the structure of the WW-USM, distancing the driving frequency from its neighboring resonant frequencies. This guarantees that other modes do not interfere with the traveling wave mode. The motor stator designed in this study consisted of a stainless wedge, a piezoelectric tube and a stainless steel base. The piezoelectric tube was made by the powder metallurgy method, as it is not suitable to alter the structure using secondary machining processing. Because the piezoelectric tube supplier could not meet our design needs, we adjusted the upper segment height H of the stainless base to achieve acceptable modal separation.

In the structure design stage, a USM designer usually judges the quality of modal separation based on the structural frequency response function. Structural adjustment occasionally causes a significant change in a specific mode's resonance frequency. Intersections of different modes appear in the frequency range of interest. However, it is not possible to guarantee which mode the neighboring resonance frequency belongs to. The dispersion curve in Fig. 7 provides a two dimensional view of the modal separation between the mode shape and the resonance frequency. This view is better than the spectrum of the frequency response because the latter is an one-dimensional observation. Let us clearly search the neighboring resonance frequency respective modes, and suitably correct the adjustment of the structure. This is the most important aspect of this study, as it effectively promotes the motor's efficiency.

Most manufacturers of commercial piezoelectric products provide data sheets listing the fundamental resonant frequencies of their products. However, the products might not satisfy the demand for clear modal separation between the resonant frequencies near the driving frequency of the WW-USM. In addition, the resonant frequencies do not appear monotonically in the sequence of resonant vibration modes. Trimming the modal separation between resonant frequencies is therefore a critical issue in designing this type of motor stator. Changing the upper segment height H of the base structure significantly influences modal separation.

For longitudinal modes, torsional modes and flexural modes alike, resonant frequencies decrease as the upper segment base height H increases. However, the fundamental flexural modes with an axial mode number $m=1$ are only slightly influenced by the increased H. Since the energy carried by the fundamental flexural wave concentrates in the area near wedge tip, increasing the base height does not significantly change the resonant frequencies. For modes with an axial mode number greater than one, the wave energy widely distributes over top and underneath the stator. Heat generation induced damages will happen to the piezoelectric tube in the stator if wave energy spreads underneath. This is why the fundamental flexural mode $F(1, 4)$ was selected to drive the WW-USM in this study.

6. Conclusion

The proposed WW-USM is driven by a traveling wave consisting of two standing waves of equal amplitude and a phase difference of 90°. If the unexpected modes existence or the modes near $F(1,4)$ are excited, the WW-USM performance is not satisfactory. This causes the output torque and efficiency of the mechanical/electrical energy transformation to be lower than predicted.

The Bi-d FEA method successfully improves the performance of a WW-USM by adjusting the upper segment height H on the stainless base. Increasing the upper segment base height H from 0 to 12.5 mm effectively decreases the unexpected disturbance due to $F(2,2)$ mode by about 11.6 kHz. Simulation results show that the disturbance caused by the $F(2,2)$ mode gradually vanishes as the upper segment height H increases. The proposed design with $H=12.5$ mm has twice the rotary torque for $H=0$, and the rise time to steady state is 40% faster than the prototype with $H=0$. The rotary torque, output power and mechanical/electrical transform efficiency all improve by 50%. The design clearly represents the optimum structure of a WW-USM stator.

Experimental results indicate the motor operates as expected. However, the output torque remains too small. From the viewpoint of the performance of the flexural vibrator, increasing the pre-load and the driving voltage of the WW-USM can increase the output torque. To conserve power and improve the overall performance of the actuator, future research should identify a more suitable friction material between the rotor and the stator. This topic remains a significant future challenge for WW-USM design, as in other types of ultrasonic motors.

Acknowledgments

The authors gratefully thank the financial support from the National Science Council of the Republic of China through the Grant NSC 95-2221-E-009-008.

References

[1] P.E. Lagasse, Analysis of a dispersion free for elastic waves, IEEE Transactions on Microwave Theory and Techniques MTT-21 (1972) 225–236.
[2] P.E. Lagasse, I.M. Mason, E.A. Ash, Acoustic surface waveguides—analysis and assessment, IEEE Transactions on Microwave Theory and Techniques 21 (4) (1973) 225–236.
[3] V.V. Krylov, Propagation of wedge acoustic waves along wedges imbedded in water, IEEE Ultrasonics Symposium (1994) 793–796.
[4] V.V. Krylov, G.V. Pritchard, Experimental confirmation of the propulsion of marine vessels employing guided flexural waves in attached elastic fins, Journal of Fluids and Structures 23 (2) (2007) 297–307.
[5] V.V. Krylov, G.V. Pritchard, Experimental investigation of the aquatic propulsion caused by localized flexural wave propagation in immersed wedges and plates, Applied Acoustics 68 (1) (2007) 97–113.
[6] A.C. Hladky-Hennion, Finite element analysis of the propagation of acoustic waves in waveguides, Journal of Sound and Vibration 194 (2) (1996) 119–136.
[7] T. Sashida, T. Kenjo, An Introduction to Ultrasonic Motors, Clarendon Press, Oxford, 1993.
[8] W.H. Duan, S.T. Quek, S.P. Lim, Finite element solution for intermittent-contact problem with piezoelectric actuation in ring type USM, Finite Elements in Analysis and Design 43 (2007) 193–205.
[9] M. Kurosawa, S. Ueha, Hybrid transducer type ultrasonic motor, IEEE Transactions on Ultrasonics, Ferroelectrics, and Frequency Control 38 (2) (1991) 89–92.
[10] S. Ueha, Y. Tomikawa, M. Kurosawa, N. Nakamura, Ultrasonic Motors: Theory and Applications, Clarendon Press, Oxford, 1993.
[11] J. Satonobu, D.-K. Lee, K. Nakamura, S. Ueha, Improvement of the longitudinal vibration system for the hybrid transducer ultrasonic motor, IEEE Transactions on Ultrasonics, Ferroelectrics, and Frequency Control 47 (1) (2000) 216–221.
[12] P. Hagedorn, J. Wallaschek, Travelling wave ultrasonic motors, part I: working principle and mathematical modelling of the stator, Journal of Sound and Vibration 155 (1) (1992) 31–46.
[13] P. Hagedorn, J. Wallaschek, W. Konrad, Travelling wave ultrasonic motors, part II: a numerical method for the flexural vibrations of the stator, Journal of Sound and Vibration 168 (1) (1993) 115–122.
[14] F.-L. Wen, C.-Y. Yen, M.S. Ouyang, Thin-disk piezoceramic ultrasonic motor Part I: design and performance evaluation, Ultrasonics 41 (2003) 437–450.
[15] C.-Y. Yen, F.-L. Wen, M.S. Ouyang, Thin-disk piezoceramic ultrasonic motor part II: system construction and control, Ultrasonics 41 (2003) 451–463.
[16] F.-L. Wen, S.-C. Mou, M.S. Ouyang, Design and construction of shaft-driving type piezoceramic ultrasonic motor, Ultrasonics 43 (2004) 35–47.
[17] T. Morita, M. Kurosawa, T. Higuchi, A cylindrical micro ultrasonic motor using PZT thin film deposited by single process hydrothermal method, IEEE Transactions on Ultrasonics, Ferroelectrics, and Frequency Control 45 (5) (1998) 1178–1187.
[18] B. Koc, S. Cagatay, K. Uchino, A piezoelectric motor using two orthogonal bending modes of a hollow cylinder, IEEE Transactions on Ultrasonics, Ferroelectrics, and Frequency Control 49 (4) (2002) 495–500.
[19] O. Vyshnevskyy, S. Kovalev, J. Mehner, Coupled tangential-axial resonant modes of piezoelectric hollow cylinders and their application in ultrasonic motors, IEEE Transactions on Ultrasonics, Ferroelectrics, and Frequency Control 52 (1) (2005) 31–36.
[20] A. Iula, M. Pappalardo, A high-power traveling wave ultrasonic motor, IEEE Transactions on Ultrasonics, Ferroelectrics, and Frequency Control 53 (7) (2006) 1344–1351.
[21] A. Iula, M. Pappalardo, FE analysis and experimental characterization of a high torque travelling wave ultrasonic motor, in: Proceedings of IEEE Ultrasonic Symposium, Beijing, China, November 2008, pp. 635–638.